ChemComm

COMMUNICATION

View Article Online
View Journal | View Issue

Cite this: *Chem. Commun.*, 2021, 57, 8981

Received 10th July 2021,
Accepted 3rd August 2021

DOI: 10.1039/d1cc03661k

rsc.li/chemcomm

Electrochemical synthesis of annealing-free and highly stable black-phase $CsPbI_3$ perovskite†

Chuyun Ding,‡[a] Xi Chen,‡[a] Tianju Zhang,‡[bc] Chaocheng Zhou,[ad] Xiaolin Liu,*[a] Jun Wang,*[bce] Jia Lin*[a] and Xianfeng Chen[df]

All-inorganic $CsPbI_3$ halide perovskite has become a hot research topic for applications in next-generation optoelectronic devices. However, the main limitations are the high-temperature synthesis and poor phase stability. In this study, we demonstrate a unique solution-phase strategy for the low-temperature preparation of black-phase $CsPbI_3$ by *in situ* electrochemistry. By controllable adjustment of the electrochemical growth process, annealing-free black-phase $CsPbI_3$ can be synthesized. The black-phase $CsPbI_3$ showed high-purity red photoluminescence at approximately 690 nm with ultra-high environmental stability for up to 11 days at a high relative humidity of 70%. The underlying mechanisms of the formation of the highly stable black-phase $CsPbI_3$ at room temperature have been discussed in this study. The results provide a new platform for the large scale, low-temperature, and convenient synthesis of black-phase $CsPbI_3$ perovskite.

Halide perovskite is a promising optoelectronic material with excellent characteristics, such as high absorption coefficient, adjustable bandgap, small effective carrier mass, and long carrier diffusion length.[1,2] For traditional hybrid halide perovskites, volatile and hygroscopic organic cations lead to poor stability at high temperature and under ambient conditions, hindering their further development.[3] Thus, all-inorganic $CsPbX_3$ (X = Cl, Br, I) perovskites have received extensive attention from researchers for their unique thermal stability.[4] Among them, the cubic black-phase (α-phase) $CsPbI_3$ exhibits a suitable bandgap of 1.73 eV, which is ideal for photovoltaic and light-emitting applications.[5–8] However, owing to its structural characteristics, the preparation of black-phase $CsPbI_3$ requires high-temperature annealing. In addition, it exhibits poor phase stability under ambient conditions, and is easily transformed into a thermodynamically stable non-perovskite yellow-phase (δ-phase).[9,10] These factors bring great challenges to its applications in optoelectronic devices.

Various strategies have been developed to improve its environmental stability. For example, molecular additive modification controls the diffusion of precursor ions and can retard nucleation and crystallization to achieve black-phase $CsPbI_3$ films with enhanced stability.[11–13] Structural distortion to form low-symmetry β- or γ-phase has been reported to realize the black-phase $CsPbI_3$ at relatively low temperatures.[14,15] Dimensionality reduction, such as quantum dots or nanocrystals, can also significantly inhibit the appearance of the non-perovskite phase.[16–19] The infiltration of $CsPbI_3$ within pre-synthesized porous oxides, such as Al_2O_3, SiO_2, and TiO_2, has been proposed to guide the post perovskite growth and protect it from contacting water molecules; thus, improving the stability.[20–22] These methods generally require high-temperature annealing to obtain the black-phase $CsPbI_3$. In addition, the experimental procedure is complicated and the obtained black-phase $CsPbI_3$ is not stable in a highly humid environment.

To achieve the direct synthesis of the highly stable black-phase $CsPbI_3$ under ambient conditions, eliminate high-temperature treatment, and meet the needs of large-scale preparation, new strategies need to be explored. The electrochemical method has the advantages of controllable adjustment of the growth, structures, and properties of materials by changing the reaction conditions such as voltage, electrolyte composition and temperature, and reaction duration. In addition, the electrochemical synthesis is suitable for

[a] *Department of Physics, Shanghai Key Laboratory of Materials Protection and Advanced Materials in Electric Power, Shanghai University of Electric Power, Shanghai 200090, China. E-mail: xlliu@shiep.edu.cn, jlin@shiep.edu.cn*
[b] *Laboratory of Micro-Nano Optoelectronic Materials and Devices, Key Laboratory of Materials for High-Power Laser, Shanghai Institute of Optics and Fine Mechanics, Chinese Academy of Sciences, Shanghai 201800, China. E-mail: jwang@siom.ac.cn*
[c] *Center of Materials Science and Optoelectronic Engineering, University of Chinese Academy of Sciences, Beijing 100049, China*
[d] *State Key Laboratory of Advanced Optical Communication Systems and Networks, School of Physics and Astronomy, Shanghai Jiao Tong University, Shanghai 200240, China*
[e] *CAS Center for Excellence in Ultra-intense Laser Science, Shanghai 201800, China*
[f] *Collaborative Innovation Center of Light Manipulation and Applications, Shandong Normal University, Jinan 250358, China*

† Electronic supplementary information (ESI) available: Experimental section, additional figures and others. See DOI: 10.1039/d1cc03661k

‡ Chuyun Ding, Xi Chen, and Tianju Zhang contributed equally to this study and share the first authorship.

mass production, with the prospect of large-scale applications. Electrochemistry-assisted preparation of $MAPbI_3$ and $CsPbBr_3$ perovskite films has recently been reported for highly efficient perovskite solar cells.[23,24] This method might also be utilized to develop black-phase $CsPbI_3$, although it is prone to phase change at room temperature compared with $MAPbI_3$ and $CsPbBr_3$.

In this study, we report the *in situ* electrochemical synthesis of black-phase $CsPbI_3$ at room temperature to eliminate high-temperature processing and stabilize the black phase. The electrochemical reaction is conducted in air at room temperature in an electrolyte containing the perovskite precursors, which makes the synthesis of black-phase $CsPbI_3$ cost effective and scalable. The overall process can be divided into two steps. In step **I**, porous TiO_2 was prepared and Pb^{2+} was introduced simultaneously by anodic oxidation in a Pb^{2+}-containing electrolyte.[25] In step **II**, the obtained Pb^{2+}-infiltrated TiO_2 reacted with Cs^+ and I^- to form a $CsPbI_3$ nanocomposite. The sample showed red photoluminescence (PL) with a peak at approximately 690 nm under ultraviolet (UV) excitation, indicating the effective formation of black-phase $CsPbI_3$. When exposed to highly humid air (relative humidity RH = 70%), red emission was maintained for more than 11 days.

The preparation process was conducted under ambient conditions and described in two steps. In step **I**, Pb^{2+} was introduced into porous TiO_2 *via in situ* electrochemical oxidation for different durations. The optimized applied voltage and F^- concentration in the electrolyte were determined to be 30 V and 0.5 wt%, respectively. The results showed that a high voltage or F^- concentration would lead to severe corrosion of the Ti sheet; however, porous TiO_2 could not form if the voltage was too low. For Pb^{2+}, it was discovered that excess F^- and Pb^{2+} in the electrolyte would form an insoluble white precipitate of PbF_2. Thus, a saturated PbI_2 concentration of 0.01 mol L^{-1} was selected. In step **II**, the anodized Ti sheet was soaked in a CsI/methanol solution with different CsI concentrations, promoting the combination of Pb^{2+} and CsI to form $CsPbI_3$. The optimized soaking temperature and time were found to be 50 °C and 20 min, respectively, to achieve a complete reaction. The synthesis details are given in the ESI.† The resulting samples are referred to by their anodization time and CsI concentration as "anodization time-CsI concentration", *i.e.*, sample 12 h–8 mg ml^{-1} was anodized for 12 h with a CsI concentration of 8 mg ml^{-1}. The schematic diagram of the experimental process is shown in Fig. 1.

The morphology of the nanocomposite was investigated using scanning electron microscopy (SEM). TiO_2 porous structures were obtained, as shown in Fig. S1 (ESI†). Energy-dispersive X-ray (EDX) elemental mapping showed that Cs, Pb, I, O, and Ti elements were uniformly distributed on the surface, and the ratio of Pb : I was approximately 1 : 3 (Fig. S2, ESI†). The composition and valence states were also characterized using X-ray photoelectron spectroscopy (XPS). The survey spectrum and high-resolution spectra of Cs 3d, Pb 4f, and I 3d are shown in Fig. 2. The two symmetric peaks at binding energies of 738.1 and 724.2 eV with a separation of 13.9 eV were attributed to Cs $3d_{3/2}$ and $3d_{5/2}$ energy levels, respectively.[26] The spectrum of Pb 4f shows $4f_{5/2}$ (143.3 eV) and $4f_{7/2}$ (138.3 eV) peaks with a separation of 5.0 eV, indicating the formation of Pb^{2+}

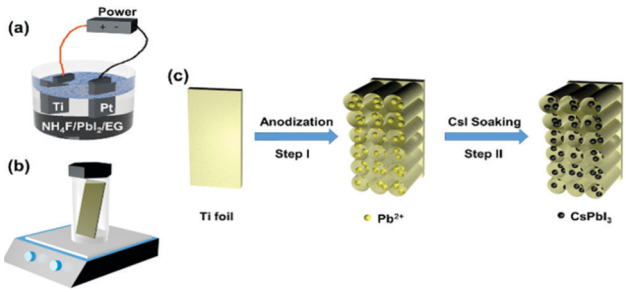

Fig. 1 Schematic diagram of the experimental process. (a) *In situ* incorporation of Pb^{2+} into porous TiO_2 by electrochemical anodization; (b) conversion of Pb^{2+} to $CsPbI_3$ by immersion in CsI/methanol solution; (c) formation of black-phase $CsPbI_3$ in porous TiO_2 after the two steps.

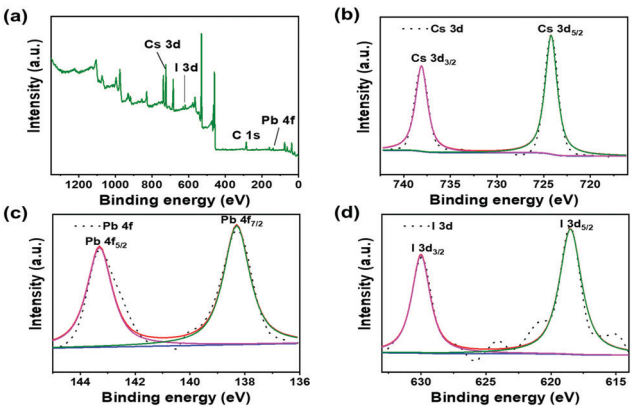

Fig. 2 XPS spectra of black-phase $CsPbI_3$. (a) Survey spectrum and core level spectra of (b) Cs 3d, (c) Pb 4f, and (d) I 3d.

ions.[27] The double peaks of I $3d_{3/2}$ (630.0 eV) and $3d_{5/2}$ (618.5 eV) in the I 3d spectrum were attributed to I^-. The powder X-ray diffraction (PXRD) pattern of the composite matched well with the calculated γ-$CsPbI_3$ pattern with only additional Cs_2TiF_6 peaks (Fig. S3, ESI†), which clearly proved the effective formation of the black-phase $CsPbI_3$ by electrochemical reaction at room temperature.

Photographs of the as-prepared 12 h–8 mg ml^{-1} sample on the Ti sheet and that under UV excitation are shown in Fig. 3a, which exhibits a uniform red PL emission in the entire area (with a sample size of approximately 2 cm^2). This indicates the uniform formation of black-phase $CsPbI_3$ on the surface without additional post-synthesis heat treatment. However, after high-temperature annealing at 320 °C, the sample became non-emissive, which is possibly due to the formation of a $CsPbI_3$–TiO_2 heterojunction resulting in PL quenching.[28] We found that the sample prepared in N_2 atmosphere was not emissive under UV excitation due to the formation of the Cs_4PbI_6 intermediate under the CsI-rich soaking condition.[29] The intermediate can be transformed into the black-phase $CsPbI_3$ after reacting with water molecules in air; thus, the sample gradually presented a red PL emission when exposed to humid air.

The PL spectrum of the 12 h–8 mg ml^{-1} sample excited by a CW laser is shown in Fig. 3b. The peak position is located at approximately 690 nm, showing a 10 nm blue shift compared

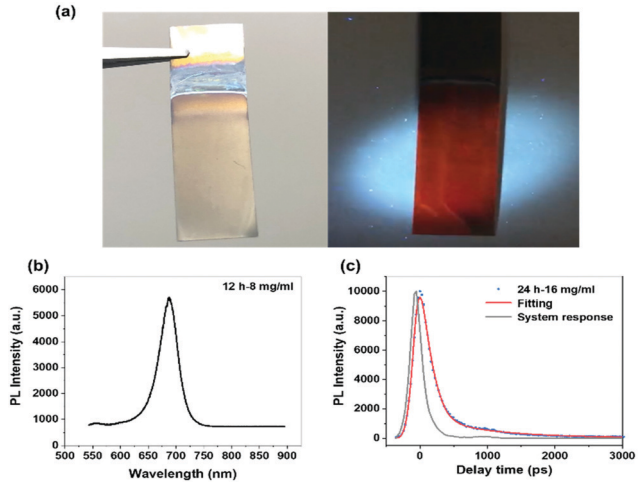

Fig. 3 PL and TRPL of black-phase $CsPbI_3$. (a) Photographs of the 12 h–8 mg ml^{-1} sample on a Ti sheet containing black-phase $CsPbI_3$ under (left) normal light and (right) UV excitation. The nanocomposite shows uniform red PL emission in the entire sample area (size of approximately 2 cm^2). (b) Room-temperature PL spectrum and (c) TRPL decay curves.

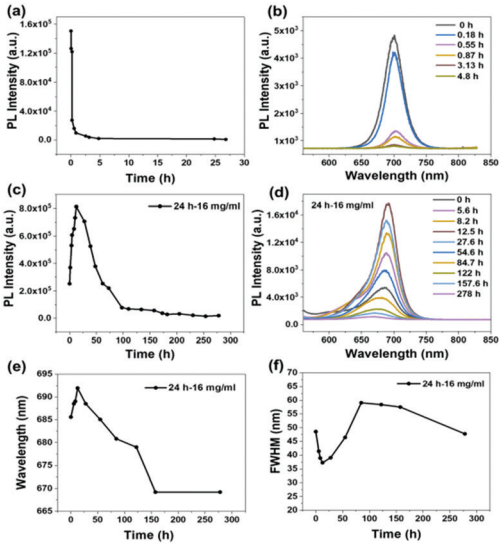

Fig. 4 Variation of the PL spectra of black-phase $CsPbI_3$ with time under highly humid conditions (RH = 70%). (a) Tracking of PL intensity with time and (b) corresponding PL spectra of reference sample **C**. Variation of (c) PL intensity, (d) PL spectra, (e) peak position, and (f) FWHM with time of the 24 h–16 mg ml^{-1} sample.

with that of thin-film $CsPbI_3$ at approximately 700 nm. The blue shift indicated the formation of small-sized $CsPbI_3$ crystals,[30] leading to a large surface area. The total energy of the black phase was smaller than the yellow phase, and thus the black-phase $CsPbI_3$ became thermodynamically more stable. We can deduce that the crystal size was approximately 16 nm, according to the previously reported results (Fig. S4, ESI†). Besides, a small PL peak was found at approximately 560 nm, which is primarily caused by TiO_2 oxygen vacancies.

The carrier dynamics were characterized using time-resolved PL (TRPL) spectroscopy, as shown in Fig. 3c. The decay curve was fitted by a biexponential function: $y = A_1\exp(-x/\tau_1) + A_2\exp(-x/\tau_2) + y_0$, where τ_1 and τ_2 are the fast and slow components of the decay lifetime, respectively.[31] Details of the fitting parameters can be found in Table S1 (ESI†). The results showed that the values of τ_1 and τ_2 were 0.11 and 0.88 ns, respectively. The short PL decay lifetime was due to the close contact of $CsPbI_3$ with TiO_2, which accelerated charge transfer.[28] The obtained black-phase $CsPbI_3$ exhibited high phase stability that remained emissive up to 157 h of exposure to humid air (RH = 70%) without encapsulation (Fig. S5, ESI†).

For comparison, reference sample **A** was synthesized by a typical two-step process, consisting of spin-coating PbI_2 thin films and soaking in the CsI solution. The resulting **A** sample was not emissive under UV excitation, indicating the formation of yellow-phase $CsPbI_3$,[32] as shown in Fig. S6 (ESI†). If Pb^{2+} was introduced *ex situ* (reference sample **B**, by pre-anodizing Ti sheet in NH_4F/EG, soaking in NH_4F/PbI_2/EG, and then soaking in CsI/methanol), the sample surface was not smooth, and the PL emission was not uniform, as shown in Fig. S7 (ESI†). The PL intensity and phase stability were also not as good as those obtained by *in situ* introduction of Pb^{2+}. Direct filling of $CsPbI_3$ precursor solution into porous TiO_2 was also attempted (reference sample **C**), which resulted in the complete transformation of black-phase to yellow-phase in humid air (RH = 70%) within 5 h, as shown in Fig. 4a and b. The results indicate that the electrochemical process changed the nucleation dynamics and formation energy of $CsPbI_3$, which promoted the crystallization of the specific black phase and enhanced stability.

The synthesis parameters of step **I** were modified to optimize the $CsPbI_3$ phase stability. As shown in Fig. S8 (ESI†), the PL lifetime of the 24 h–8 mg ml^{-1} sample was longer than that of the 12 h–8 mg ml^{-1} and 36 h–8 mg ml^{-1} samples at the same CsI concentration, indicating that the optimized reaction time was 24 h. If the anodization time was too short, the amount of Pb^{2+} required to fill the porous TiO_2 was insufficient. However, if the anodization time was too long, the top of the porous TiO_2 was dissolved and blocked, which impeded further reaction of Pb^{2+} with CsI.

The influence of CsI concentration in step **II** was also investigated. The results showed that the 24 h–16 mg ml^{-1} sample had the longest PL lifetime compared with that of the 24 h–8 mg ml^{-1} and 24 h–4 mg ml^{-1} samples (Fig. 4c and Fig. S8, ESI†). For the as-prepared 24 h–16 mg ml^{-1} sample, the peak PL intensity of $CsPbI_3$ gradually increased with time when exposed to air. The maximum value was achieved at 12.5 h (intensity increased by about 322% from the initial value) and then gradually weakened. The enhanced PL intensity was caused by the phase transition of Cs_4PbI_6 triggered by moisture in air, increasing the number of $CsPbI_3$ crystals. The transformation process also existed in the 12 h–8 mg ml^{-1}, 24 h–8 mg ml^{-1}, 36 h–8 mg ml^{-1}, and 24 h–4 mg ml^{-1} samples. The time for the moisture to complete Cs_4PbI_6 phase transformation was shorter and the transition was not obvious in these samples, since the number of intermediates was less than that of the 24 h–16 mg ml^{-1} sample.[33]

After 50 h of exposure to humid air (RH = 70%), the PL intensity of the 24 h–16 mg ml^{-1} sample remained the same as its initial value. The red emission can still be observed after 11 days (Fig. S5, ESI†), indicating high phase stability compared

with previous reports (Table S2, ESI†). Fig. 4d shows the PL spectra of the 24 h–16 mg ml^{-1} sample monitored from 0 to 278 h. The emission peak of $CsPbI_3$ was first red-shifted from 685 to 691 nm, and then blue-shifted to 669 nm, as shown in Fig. 4e. The corresponding FWHM changed from 48 to 37 nm and then to 47 nm, as shown in Fig. 4f. The initial PL originated from small crystals formed at the early stage, while the degradation of the small $CsPbI_3$ crystals led to the red shift. The slight blue shift may be attributed to the size reduction due to surface etching caused by exposure to air over a long period.

The mechanism of integration of $CsPbI_3$ with TiO_2 and significantly improved phase stability were further investigated. In the electrochemical reaction process, I^- ions lost electrons and formed I_2 at the anode, which quickly dissolved in the electrolyte to form HI. This caused the formation of yellow liquid near the anode during the reaction. It is possible that Pb^{2+} ions reacted with the anions (such as F^-) and formed a negatively charged micelle, which increasingly accumulated at the anode, and were trapped into porous TiO_2 due to cation-exchange reaction.[21,34] Subsequently, the embedded Pb^{2+} fully reacted with Cs^+ and I^- in methanol to form $CsPbI_3$. The stable black-phase primarily originates from the following two factors. First, small-sized $CsPbI_3$ grains were protected by the porous TiO_2, slowing down the transition from the black phase to the yellow phase.[22] Second, the soaking process was conducted in a CsI-rich environment, which can stabilize the black phase over the yellow phase.[35] Further improvement of the water stability and one-step electrochemical synthesis may be required for future investigation.

In summary, photoactive black-phase $CsPbI_3$ was prepared by introducing $CsPbI_3$ into porous TiO_2 with a two-step solution strategy at room temperature. By optimizing the parameters, the $CsPbI_3$ nanocomposite stability was significantly improved under highly humid conditions monitored by PL. This study provides a new strategy to stabilize black-phase $CsPbI_3$ at room temperature under ambient conditions, which has potential applications in future photovoltaics, light-emitting diodes, and other optoelectronic devices.

The work was supported by the National Natural Science Foundation of China (Grant No. 61875119 and 61975221), the Program for Professor of Special Appointment (Eastern Scholar) at Shanghai Institutions of Higher Learning, Shanghai Rising-Star Program (Grant No. 19QA1404000), Youth Innovation Promotion Association CAS (2016237), Shanghai Talent Development Fund, the "Chen Guang" project supported by Shanghai Municipal Education Commission and Shanghai Education Development Foundation (Grant No. 18CG63), the Strategic Priority Research Program of CAS (No. XDB16030700 and XDB43010303), and Shanghai Science and Technology International Cooperation Fund (No. 19520710200).

Conflicts of interest

There are no conflicts of interest to declare.

References

1 A. K. Jena, A. Kulkarni and T. Miyasaka, *Chem. Rev.*, 2019, **119**, 3036–3103.
2 L. Chouhan, S. Ghimire, C. Subrahmanyam, T. Miyasaka and V. Biju, *Chem. Soc. Rev.*, 2020, **49**, 2869–2885.
3 C. Liu, Y. Yang, X. Liu, Y. Ding, Z. Arain, X. Li, Y. Li, Z. Zhou, S. Dai and M. K. Nazeeruddin, *J. Mater. Chem. A*, 2020, **8**, 10226–10232.
4 Z. Zeng, J. Zhang, X. Gan, H. Sun, M. Shang, D. Hou, C. Lu, R. Chen, Y. Zhu and L. Han, *Adv. Energy Mater.*, 2018, **8**, 1801050.
5 B. Jeong, H. Han, Y. J. Choi, S. H. Cho, E. H. Kim, S. W. Lee, J. S. Kim, C. Park, D. Kim and C. Park, *Adv. Funct. Mater.*, 2018, **28**, 1706401.
6 J. Lin, M. Lai, L. Dou, C. S. Kley, H. Chen, F. Peng, J. Sun, D. Lu, S. A. Hawks, C. Xie, F. Cui, A. P. Alivisatos, D. T. Limmer and P. Yang, *Nat. Mater.*, 2018, **17**, 261–267.
7 G. Li, R. Gao, Y. Han, A. Zhai, Y. Liu, Y. Tian, B. Tian, Y. Hao, S. Liu and Y. Wu, *Photon. Res.*, 2020, **8**, 1862–1874.
8 Z. Liu, C. Wang, Z. Hu, J. Du, J. Yang, Z. Zhang, T. Shi, W. Liu, X. Tang and Y. Leng, *Photon. Res*, 2020, **8**, A31–A38.
9 X. Li, F. Cao, D. Yu, J. Chen, Z. Sun, Y. Shen, Y. Zhu, L. Wang, Y. Wei and Y. Wu, *Small*, 2017, **13**, 1603996.
10 Y. Zhao, F. Ma, F. Gao, Z. Yin, X. Zhang and J. You, *Photon. Res*, 2020, **8**, A1–A15.
11 L. Wang, B. Liu, X. Zhao, H. V. Demir, H. Gu and H. Sun, *ACS Appl. Mater. Interfaces*, 2018, **10**, 19828–19835.
12 L. Liang, Z. Li, F. Zhou, Q. Wang, H. Zhang, Z. Xu, L. Ding, S. F. Liu and Z. Jin, *J. Mater. Chem. A*, 2019, **7**, 26776–26784.
13 Y. Zhu, J. Zhao, G. Yang, X. Xu and G. Pan, *Nanoscale*, 2020, **12**, 7712–7719.
14 Y. Wang, M. I. Dar, L. K. Ono, T. Zhang, M. Kan, Y. Li, L. Zhang, X. Wang, Y. Yang and X. Gao, *Science*, 2019, **365**, 591–595.
15 B. Zhao, S.-F. Jin, S. Huang, N. Liu, J.-Y. Ma, D.-J. Xue, Q. Han, J. Ding, Q.-Q. Ge and Y. Feng, *J. Am. Chem. Soc.*, 2018, **140**, 11716–11725.
16 A. Swarnkar, A. R. Marshall, E. M. Sanehira, B. D. Chernomordik, D. T. Moore, J. A. Christians, T. Chakrabarti and J. M. Luther, *Science*, 2016, **354**, 92–95.
17 E. M. Sanehira, A. R. Marshall, J. A. Christians, S. P. Harvey, P. N. Ciesielski, L. M. Wheeler, P. Schulz, L. Y. Lin, M. C. Beard and J. M. Luther, *Sci. Adv.*, 2017, **3**, eaao4204.
18 F. Liu, Y. Zhang, C. Ding, S. Kobayashi, T. Izuishi, N. Nakazawa, T. Toyoda, T. Ohta, S. Hayase and T. Minemoto, *ACS Nano*, 2017, **11**, 10373–10383.
19 K. M. Sim, A. Swarnkar, A. Nag and D. S. Chung, *Laser Photonics Rev.*, 2018, **12**, 1700209.
20 S. Ma, S. H. Kim, B. Jeong, H. C. Kwon, S. C. Yun, G. Jang, H. Yang, C. Park, D. Lee and J. Moon, *Small*, 2019, **15**, 1900219.
21 M. Xing, B. Chen, J. Feng, W. Xu, Y. Bai, Y. Zhou, C. Dong, H. Zhong, J. Zhang and Y. Yin, *Chem*, 2019, **5**, 2195–2214.
22 Z. J. Li, E. Hofman, J. Li, A. H. Davis, C. H. Tung, L. Z. Wu and W. Zheng, *Adv. Funct. Mater.*, 2018, **28**, 1704288.
23 X. Wang, S. Abbasi, D. Zhang, J. Wang, Y. Wang, Z. Cheng, H. Liu and W. Shen, *ACS Appl. Mater. Interfaces*, 2020, **12**, 50455–50463.
24 Z. Cheng, D. Ding, J. Song, F. Liu, T. Wang, C. Hu, L. Ba, J. Wang, H. Liu and W. Shen, *Adv. Funct. Mater.*, 2020, **30**, 2004652.
25 W. Zhu, Y. Liu, A. Yi, M. Zhu, W. Li and N. Fu, *Electrochim. Acta*, 2019, **299**, 339–345.
26 J. Y. Sun, F. T. Rabouw, X. F. Yang, X. Y. Huang, X. P. Jing, S. Ye and Q. Y. Zhang, *Adv. Funct. Mater.*, 2017, **27**, 1704371.
27 Z. Zhang, L. Shen, H. Zhang, L. Ding, G. Shao, X. Liang and W. Xiang, *Chem. Eng. J.*, 2019, **378**, 122125.
28 Z. Zheng, F. Zhuge, Y. Wang, J. Zhang, L. Gan, X. Zhou, H. Li and T. Zhai, *Adv. Funct. Mater.*, 2017, **27**, 1703115.
29 H. Hu, L. Wu, Y. Tan, Q. Zhong, M. Chen, Y. Qiu, D. Yang, B. Sun, Q. Zhang and Y. Yin, *J. Am. Chem. Soc.*, 2018, **140**, 406–412.
30 Q. Zhao, A. Hazarika, L. T. Schelhas, J. Liu, E. A. Gaulding, G. Li, M. Zhang, M. F. Toney, P. C. Sercel and J. M. Luther, *ACS Energy Lett.*, 2019, **5**, 238–247.
31 J. Chen, C. Zhang, X. Liu, L. Peng, J. Lin and X. Chen, *Photon. Res*, 2021, **9**, 151–170.
32 M. Lai, Q. Kong, C. G. Bischak, Y. Yu, L. Dou, S. W. Eaton, N. S. Ginsberg and P. Yang, *Nano Res.*, 2017, **10**, 1107–1114.
33 D. Lu, Y. Zhang, M. Lai, A. Lee, C. Xie, J. Lin, T. Lei, Z. Lin, C. S. Kley and J. Huang, *Nano Lett.*, 2018, **18**, 6967–6973.
34 X. Li, Y. Wang, H. Sun and H. Zeng, *Adv. Mater.*, 2017, **29**, 1701185.
35 R. X. Yang and L. Z. Tan, *J. Chem. Phys.*, 2020, **152**, 034702.

